JACS
JOURNAL OF THE AMERICAN CHEMICAL SOCIETY
Cite This: J. Am. Chem. Soc. 2018, 140, 1409−1414
Article
pubs.acs.org/JACS

Control of Amphiphile Self-Assembly via Bioinspired Metal Ion Coordination

Abigail S. Knight,*[,†] Josefin Larsson,[†] Jing M. Ren,[†] Raghida Bou Zerdan,[†] Shay Seguin,[†] Remy Vrahas,[†] Jianfang Liu,[§] Gang Ren,[§] and Craig J. Hawker*[,†,‡]

[†]California NanoSystems Institute and Materials Research Laboratory and [‡]Materials Department and Department of Chemistry and Biochemistry, University of California, Santa Barbara, California 93106, United States

[§]The Molecular Foundry, Lawrence Berkeley National Laboratory, Berkeley, California 94720, United States

Supporting Information

ABSTRACT: Inspired by marine siderophores that exhibit a morphological shift upon metal coordination, hybrid peptide−polymer conjugates that assemble into different morphologies based on the nature of the metal ion coordination have been designed. Coupling of a peptide chelator, hexahistidine, with hydrophobic oligostyrene allows a modular strategy to be established for the efficient synthesis and purification of these tunable amphiphiles (oSt(His)$_6$). Remarkably, in the presence of different divalent transition metal ions (Mn, Co, Ni, Cu, Zn, and Cd) a variety of morphologies were observed. Zinc(II), cobalt(II), and copper(II) led to aggregated micelles. Nickel(II) and cadmium(II) produced micelles, and multilamellar vesicles were obtained in the presence of manganese(II). This work highlights the significant potential for transition metal ion coordination as a tool for directing the assembly of synthetic nanomaterials.

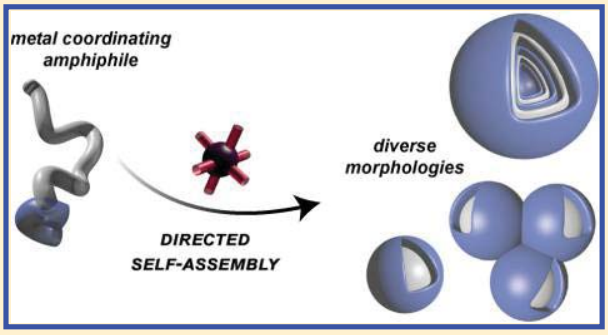

INTRODUCTION

Living organisms exploit a variety of stimuli to create nanoscale, responsive materials leading to complex macroscale functions. Structural change in response to a stimulus is critical for such functions (e.g., the release of a signaling molecule in a cascade or active transport across a membrane). Significantly, these dynamic responses allow for an array of structures/functions to be derived from a limited set of building blocks. In the pursuit of synthetic nanomaterials with comparable functionality, a toolbox of strategies including materials that respond to light,[1] pH,[2] temperature,[3] and chemical[4] stimuli has been developed. These strategies provide a valuable foundation for the development of responsive materials, but thus far they are largely limited to generating structures that interchange between two morphologies in response to various stimuli.

Transition metal ions are a unique tool for engineering responsive character based on their various binding stoichiometries and geometries, allowing a single material to have a diverse set of responses to different metal ions. This allows structural control in small molecules[5−8] and proteins,[9−11] with the dynamic nature of the coordination bonds being utilized to develop responsive films,[12,13] self-healing soft materials,[14−16] subcomponent self-assembly of polymeric materials,[17−21] and hierarchical assemblies of nanoparticles.[22,23] However, the only example of metal ion coordination leading to a controllable change in the morphology in an aqueous amphiphilic self-assembled system is demonstrated with natural siderophores that are secreted by marine bacteria.[24,25] Butler and co-workers have demonstrated that these siderophores, composed of a hydrophilic peptide-based chelator and a fatty acid tail, can undergo an unprecedented metal-induced morphology transition. In the absence of metal ions, assembly occurs to give micelles, while coordination with an excess of Fe(III), Zn(II), Cd(II), or La(III) results in dimerization of the amphiphile, inducing a substantial shift in the packing parameter and formation of new morphologies (vesicles or multilamellar vesicles).

RESULTS AND DISCUSSION

Inspired by these natural siderophore systems, we sought to design a synthetic amphiphile that forms tunable morphologies in the presence of different transition metal ions (Figure 1). A modular synthetic approach was therefore devised based on a tunable macromolecular hydrophobic unit[26−28] and a peptide chelator (Scheme 1).[29,30] Oligostyrene was selected as the hydrophobic tail due to its high hydrophobicity, chemical inertness, and glass transition temperature above room temperature. These features impart chemical and kinetic stability to the assembled structures. Hexahistidine, known to dimerize in the presence of transition metal ions,[9,31,32] was chosen as the hydrophilic chelating domain. Key features of this design are the high degree of structural control over functionality and molecular weight with the peptide component

Received: October 18, 2017
Published: January 17, 2018

DOI: 10.1021/jacs.7b11005
J. Am. Chem. Soc. 2018, 140, 1409−1414

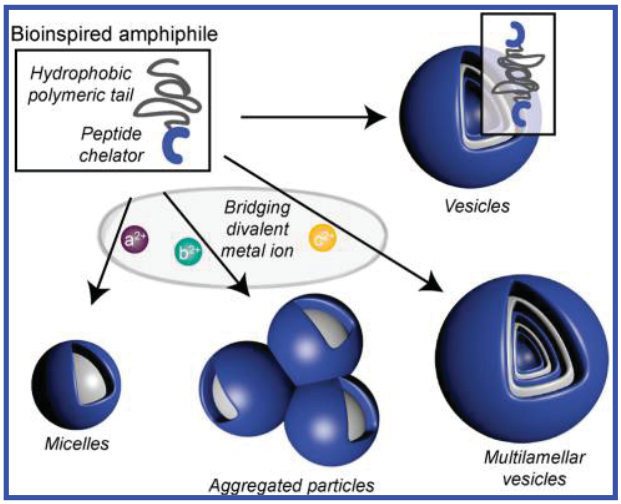

Figure 1. Schematic illustrating a single amphiphilic material that can be transformed into a variety of unique morphologies in response to the presence of different divalent transition metal ions.

Scheme 1. Modular Design Strategy for the Synthesis of oSt(His)$_6$

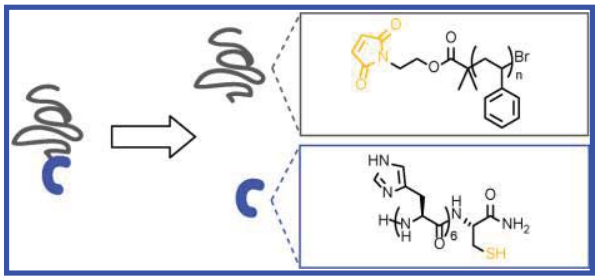

being discrete and the synthetic oligomer with a narrow distribution ($Đ$ = 1.2). This allows accurate tuning of assembly and dynamic behavior.

To probe the impact of metal ions on the assembly, a metal-free synthesis of the amphiphile was required. Therefore, efficient and metal-free chemistry (thiol−maleimide reaction) was selected to couple the peptide and oligostyrene.[33] To increase the modularity of this system, polymerization from a preformed, protected maleimide initiator was employed with atom transfer radical polymerization (ATRP),[34] allowing for a more controlled polymerization, noncoordinating chain ends, and limited *in situ* deprotection of the initiator (Figure 2a). Oligomers (degree of polymerization (DP) < 10) of styrene were targeted to provide a hydrophobic block of comparable molecular weight to drive the self-assembly of a peptide containing a hexahistidine unit with a terminal cysteine for conjugation to the maleimide. A narrow molecular weight distribution centered at a pentamer and high retention of the furan-protected chain end was confirmed by size exclusion chromatography (SEC) and ^{1}H NMR analysis (Figure 2b, Figure S3). The reactive maleimide was then exposed by heating the oligostyrene to 120 °C to release the furan followed by coupling to the peptide in DMF with HEPES buffer salt. Quenching with 0.1% trifluoroacetic acid (TFA) then gave the crude peptide−oligomer amphiphile (Figure 3a), which was initially characterized by high-performance liquid chromatography (HPLC). Isolation and purification of amphiphiles is traditionally challenging, and therefore the stoichiometry of the

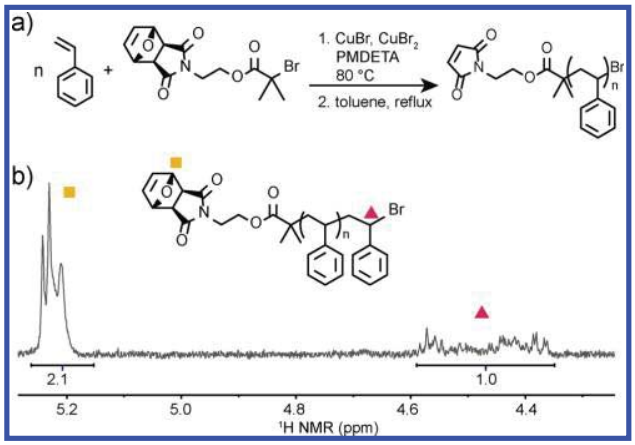

Figure 2. Synthesis of maleimide-terminated oligostyrene. (a) Synthetic scheme; (b) ^{1}H NMR spectrum of the protected-maleimide oligomer demonstrating chain end fidelity.

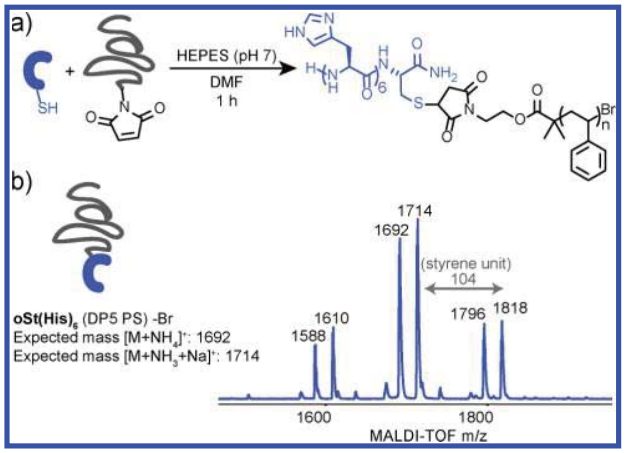

Figure 3. (a) Synthetic scheme for the coupling of oligostyrene to hexahistidine peptide via maleimide−cysteine reaction; (b) MALDI MS confirming synthesis of the peptide−polymer amphiphile. The arrow indicates the difference of a single styrene monomer unit.

coupling reaction was optimized to ensure high yields and minimization of side products. Efficient purification of the desired amphiphile from residual peptide and disulfide dimer was achieved by reverse-phase chromatography eluting with 3:1 water/acetonitrile containing 0.1% TFA to give pure oSt(His)$_6$, which was fully characterized by mass spectrometry (Figure 3b) and HPLC (Figure S5).

The critical aggregation concentration (CAC) and assembled morphology of oSt(His)$_6$ were initially studied in the absence of transition metals. The CAC was determined to be less than 10 μM by incubating oSt(His)$_6$ (concentrations of 0.3−600 μM) with solvatochromic Nile Red using a procedure similar to that described by Stupp and co-workers[35] (Figure S6). To ensure complete self-assembly of the amphiphiles, 600 μM was then selected as the concentration of oSt(His)$_6$ for all subsequent experiments. The assembly proceeded in a noncoordinating buffer,[36] HEPES (100 mM, pH 7), at 80 °C for 30 min to allow equilibration above the glass transition temperature of the styrene oligomers. Following imaging with transmission electron microscopy (TEM; cryogenic, Figure 4; negative staining, Figure 5 and Figure S7), vesicle formation was observed in the absence of any divalent metal ions. Additional characterization by dynamic light scattering (DLS,

DOI: 10.1021/jacs.7b11005
J. Am. Chem. Soc. 2018, 140, 1409−1414

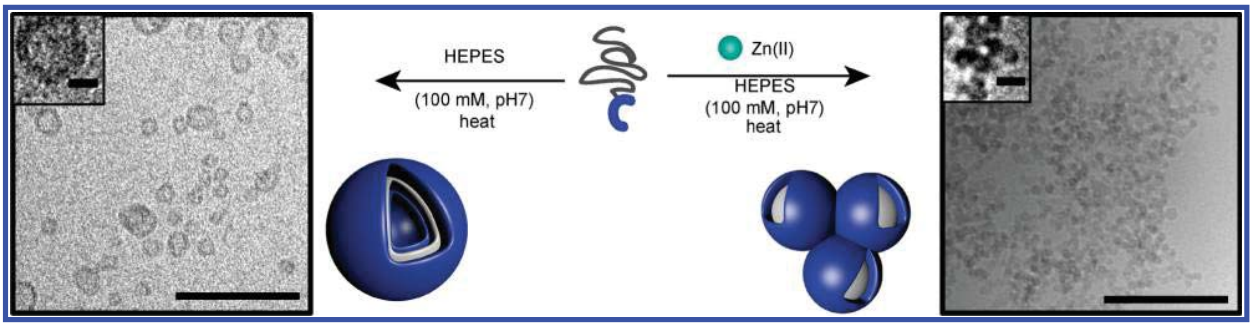

Figure 4. Schematic of the oSt(His)$_6$ and assembled structures in the absence (left) and presence (right) of Zn(II) (15 mM) in addition to cryo-TEM images. Scale bars represent 200 nm (larger image) and 20 nm (inset image).

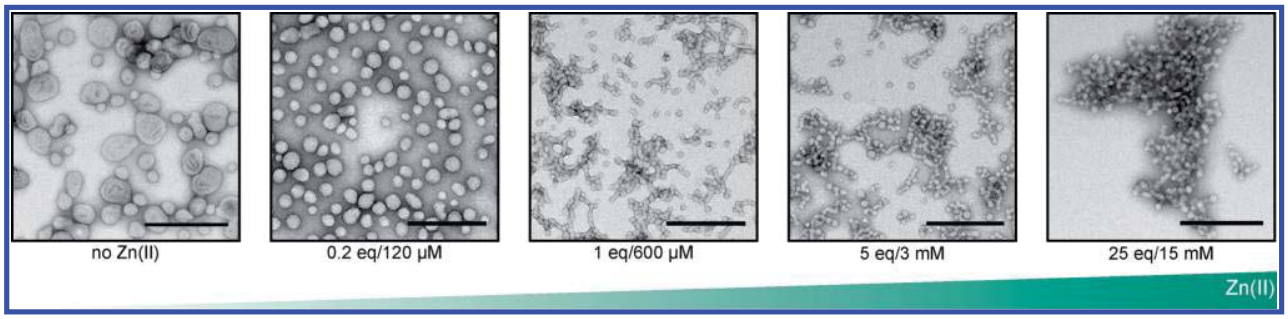

Figure 5. Varying concentrations of Zn(II) lead to different degrees of aggregation. Negative-stained TEM images of oSt(His)$_6$ (600 μM) assembled with 0−15 mM Zn(II). Negative staining was performed with uranium formate, and all scale bars represent 200 nm. All assembly was performed in buffered solution (HEPES, 100 mM, pH 7).

Figure S15) confirmed vesicle formation with only minimal aggregation. This low level of aggregation is presumably due to secondary interactions between the noncoordinating zwitterionic buffer and the positively charged peptide corona.

Zinc has been previously demonstrated to dimerize hexahistidine peptides[31] and was initially investigated for directing amphiphile assembly. An excess of Zn(II) (15 mM) was therefore added to a buffered oSt(His)$_6$ solution (600 μM oSt(His)$_6$ and 100 mM HEPES) at a neutral pH (confirmed with bromothymol blue) and assembly conducted by heating the mixture to 80 °C and slowly cooling it to room temperature. Imaging with TEM (cryogenic, Figure 4; negative staining, Figure 5 and Figure S7) revealed a definitive change in morphology. In direct contrast to the vesicles formed in the absence of transition metals, zinc induced the formation of networks of aggregated micelles. It is particularly noteworthy that the metal ion was able to both change the size of the spherical assembly and lead to network-like aggregates.

The impact of zinc concentration, temperature, ionic strength, and salt counterion on the assembly was then examined to probe the factors controlling the formation of the aggregated micelle networks. Incubating oSt(His)$_6$ with increasing concentrations of $ZnCl_2$ from 120 μM (~0.1 equiv, with respect to oSt(His)$_6$) to 15 mM (~25 equiv) results in an observable transition from vesicles to micelles to aggregated micelles (Figure 5 and Figure S8). Further characterization was performed at 15 mM Zn(II), as this provides the clearest difference in morphology when compared to the metal-free assemblies. To monitor formation of these networks, samples were heated at 40, 60, and 80 °C, all above the T_g of the oligostyrene (34 °C), and the respective morphologies characterized via TEM after different incubation times (Figure S6e). Significantly, the incorporation of micelles into the aggregated network was observed to increase with increasing temperature (Figure 6, Figure S6). For each 20 °C decrease in temperature, approximately 4 times longer was required for full incorporation into aggregated networks. Samples heated to 40 °C do not appear to assemble fully,

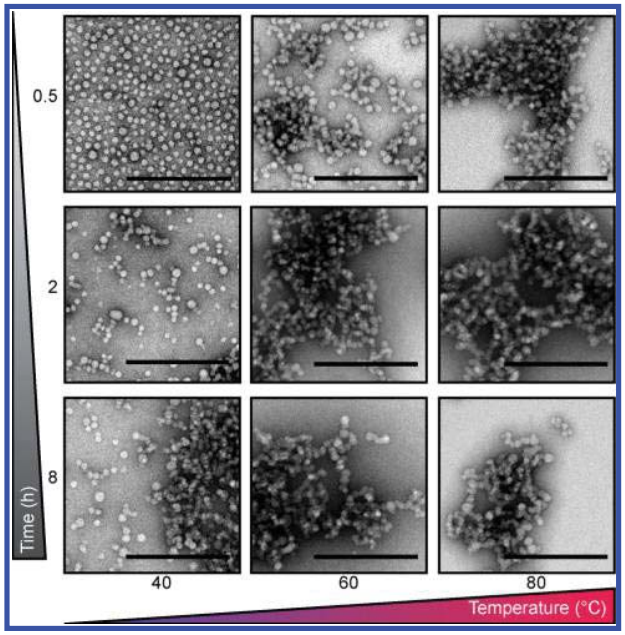

Figure 6. TEM images of oSt(His)$_6$ assembled in the presence of Zn(II) with different incubation times and temperatures. Samples negatively stained with uranium formate. All scale bars represent 200 nm.

DOI: 10.1021/jacs.7b11005
J. Am. Chem. Soc. 2018, 140, 1409−1414

likely due to this temperature being close to the reported T_g. Additionally, networks that were assembled at 80 °C (30 min) were cycled again through the same assembly conditions and demonstrated to be unaffected by reheating (Figure S8a), confirming the robustness of the final morphology. The impact of diluting the structure postassembly was tested via imaging a 10-fold dilution of the original assembled solution (Figure S8b), revealing a similar aggregated network morphology. PIPES, as an alternative to HEPES (Figure S8c), and $Zn(NO_3)_2$ and $Zn(OAc)_2$ (Figure S8e) as replacements for $ZnCl_2$, also led to the assembly of a network of aggregated micelles as visualized by TEM. Finally, when Zn(II) was replaced by noncoordinating Mg(II), spherical assemblies similar to those formed under metal-free conditions were observed (Figure S8d), reinforcing that specific interactions between the peptide domain of the amphiphile and Zn(II) lead to the network morphology.

Encouraged by the morphological change induced by Zn(II), additional transition metal ions were selected to evaluate how ions with different properties (e.g., ionic radius and coordination stoichiometry/geometry) impact assembly. Under identical conditions, assembly of $oSt(His)_6$ in the presence of Mn(II), Co(II), Ni(II), Cu(II), Cd(II), and Fe(III) was conducted, leading to a diverse array of morphologies (Figure 7, Figure S14, DLS Figure S15, negatively stained TEM Figures S9–13). Co(II)-directed assembly led to aggregated micelle networks similar to those formed in the presence of Zn(II), as visualized by cryogenic TEM. Comparable aggregation was also observed in the presence of Cu(II) with preliminary cryo-TEM visualization showing a more organized network. In contrast, Mn(II)-, Ni(II)-, and Cd(II)-directed assembly led to isolated particles as characterized by TEM and DLS, indicating that these metal ions did not induce secondary aggregation (Figure 7). Interestingly, micelles were observed in the presence of Ni(II) and Cd(II), whereas multilamellar vesicles were formed in the presence of Mn(II). A hollow core and thick corona with faint rings can be observed in the cryogenic images. Assembly in PIPES buffer allowed for clear visualization of multiple layers (Figure S13d); the particles formed in this buffer are larger, likely due to the higher ionic strength, as has been observed with phospholipids.[37] On progressing to the Fe(III) ion, only unstructured aggregates that separated from the aqueous solution were observed (Figure S14). The wide range of morphologies obtained clearly indicate that the nature of the transition metal ion and associated atomic-scale differences in coordination significantly affects nanoscale assembly, further highlighting the promise of metal binding in the development of responsive materials.

Intrigued by the observation that Ni(II) and Cd(II), ions with relatively large differences in ionic radius, both assembled into micelles, we turned our attention to the role of coordination geometry. With the exception of Mn(II), all of the ions have been demonstrated to dimerize hexahistidine;[31] therefore, we hypothesized that the structures are composed of amphiphiles binding in a 2:1 $oSt(His)_6$:metal ion ratio. Different binding geometries of these 2:1 coordination complexes may lead to the distinct assemblies visualized by cryo-TEM. For proteins engineered to contain imidazole-based binding sites, X-ray crystallography[38] has shown a tetrahedral binding geometry for Zn(II),[39] square planar for Cu(II), and octahedral for Ni(II).[40] On the basis of these reported assembly profiles,[41] we propose coordination modes for each of the morphologies (Figure 7) with square-planar (Cu(II)) and tetrahedral (Zn(II) and Co(II)) leading to aggregated micelle networks, whereas an octahedral geometry (Ni(II) and Cd(II)) with coordinated water (common in proteins[41] and observed in subcomponent assembly[20]) leads to isolated micelles. Unlike the prior transition metal ions, Mn(II) does not dimerize hexahistidine[1] and assembly is dictated by binding stoichiometry instead of geometry. To further evaluate this difference, $oSt(His)_6$ was assembled in the presence of differing stoichiometries of Mn(II) and Ni(II) with the size of the resulting nanostructures being characterized by DLS. As shown in Figure 8, only 0.5 equiv of Ni(II) are needed for micelle formation, while approximately 5.0 equiv are required for Mn(II) to form the final multilamellar vesicle. We therefore conclude that multiple Mn(II) ions are bound to each $oSt(His)_6$.

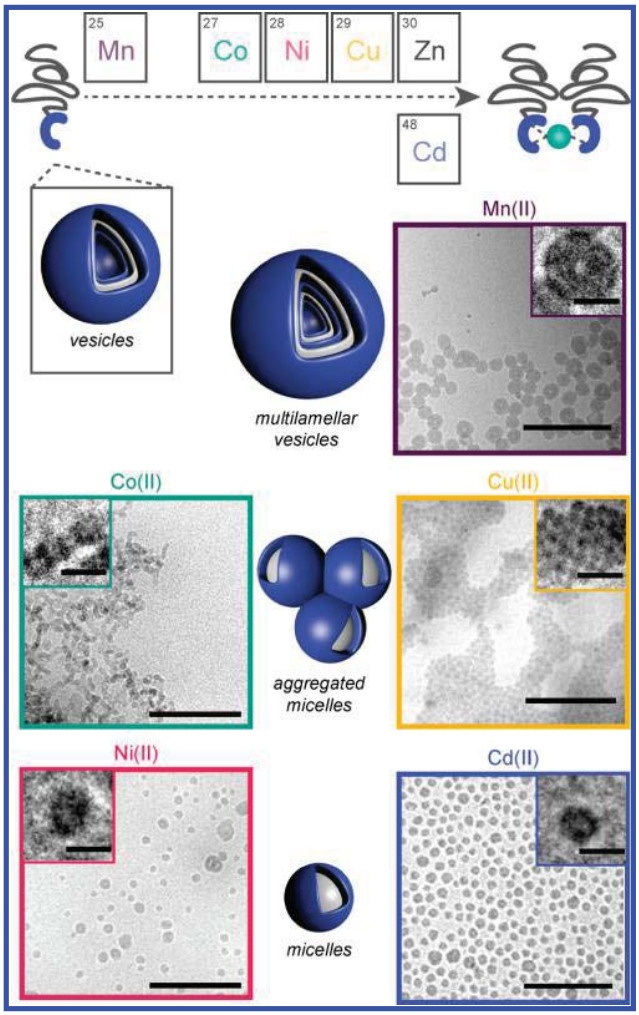

Figure 7. Assembly of $oSt(His)_6$ in the presence of divalent transition metals. Cryo-TEM images show $oSt(His)_6$ assembled in the presence of Mn(II), multilamellar vesicles; Co(II)/Cu(II), aggregated micelles; and Ni(II)/Cd(II), micelles. Scale bars represent 200 nm (larger image) and 20 nm (inset image).

CONCLUSIONS

In conclusion, we describe the formation of tunable nanoscale morphologies directed by metal ion coordination. A peptide polymer amphiphile, $oSt(His)_6$, was synthesized with a modular strategy and observed to assemble into vesicles in the absence

DOI: 10.1021/jacs.7b11005
J. Am. Chem. Soc. 2018, 140, 1409–1414

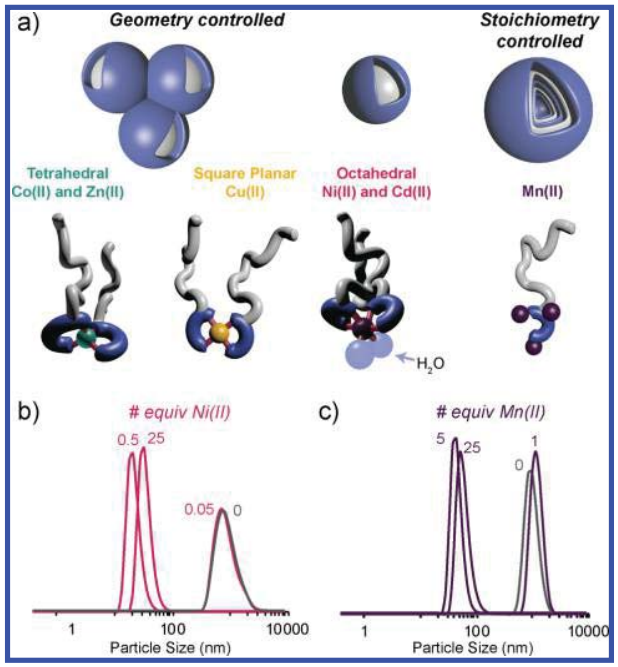

Figure 8. Proposed binding modes of oSt(His)$_6$ to divalent transition metals. (a) Illustration of the proposed coordination of oSt(His)$_6$ to divalent ions. Number distributions from DLS for oSt(His)$_6$ assembled in the presence of different numbers of equivalents of (b) Ni(II) and (c) Mn(II).

of transition metals and aggregated particles in the presence of Zn(II). The aggregation was determined to be due to the coordination of the Zn(II) ion. Aggregated particles were also observed in the presence of Co(II) and Cu(II), isolated micelles directed by Ni(II) and Cd(II) were observed, and multilamellar vesicles were formed when oSt(His)$_6$ coordinated to Mn(II). Proposed models for binding geometry and stoichiometry illustrate the control over nanoscale morphologies dictated by small differences in the nature of the transition metal ion. This design principle illustrates the wide variety of nanoscale materials that can be assembled from a well-defined oligomer–peptide amphiphile and provides an attractive avenue for the development of multistimuli-responsive nanomaterials. Future directions of this work are aimed at continuing to probe the mechanism and limitations of the role of metal ions in directing the assembly of amphiphiles.

■ ASSOCIATED CONTENT

Supporting Information

The Supporting Information is available free of charge on the ACS Publications website at DOI: 10.1021/jacs.7b11005.

Full experimental procedures and additional characterization data (PDF)

■ AUTHOR INFORMATION

Corresponding Authors

*aknight@berkeley.edu

*hawker@mrl.ucsb.edu

ORCID

Craig J. Hawker: 0000-0001-9951-851X

Notes

The authors declare no competing financial interest.

■ ACKNOWLEDGMENTS

This work was supported primarily by the National Science Foundation (MRSEC program DMR 1720256). Work at the Molecular Foundry was supported by the Office of Science, Office of Basic Energy Sciences, of the U.S. Department of Energy under Contract No. DE-AC02-05CH11231. A.S.K. was supported by a postdoctoral fellowship from the Arnold and Mabel Beckman Foundation. J.M.R. thanks the Victorian Endowment for Science, Knowledge and Innovation (VESKI) for a postdoctoral fellowship.

■ REFERENCES

(1) Coleman, A. C.; Beierle, J. M.; Stuart, M. C.; Maciá, B.; Caroli, G.; Mika, J. T.; van Dijken, D. J.; Chen, J.; Browne, W. R.; Feringa, B. L. *Nat. Nanotechnol.* **2011**, *6*, 547–552.

(2) Jang, S. G.; Audus, D. J.; Klinger, D.; Krogstad, D. V.; Kim, B. J.; Cameron, A.; Kim, S.-W.; Delaney, K. T.; Hur, S.-M.; Killops, K. L.; Fredrickson, G. H.; Kramer, E. J.; Hawker, C. J. *J. Am. Chem. Soc.* **2013**, *135*, 6649–6657.

(3) Moughton, A. O.; O'Reilly, R. K. *Chem. Commun.* **2010**, *46* (7), 1091–1093.

(4) Yan, Q.; Zhao, Y. *Angew. Chem., Int. Ed.* **2013**, *52*, 9948–9951.

(5) Sato, S.; Murase, T.; Fujita, M. *Supramolecular Chemistry: From Molecules to Nanomaterials*; John Wiley & Sons, Ltd: Hoboken, 2012.

(6) Geng, Y.; Wang, X.-J.; Chen, B.; Xue, H.; Zhao, Y.-P.; Lee, S.; Tung, C.-H.; Wu, L.-Z. *Chem. - Eur. J.* **2009**, *15*, 5124–5129.

(7) Li, L.; Ke, C.-F.; Zhang, H.-Y.; Liu, Y. *J. Org. Chem.* **2010**, *75*, 6673–6676.

(8) Xiao, Z.-Y.; Zhao, X.; Jiang, X.-K.; Li, Z.-T. *Chem. Mater.* **2011**, *23*, 1505–1511.

(9) Van Eldijk, M. B.; Schoonen, L.; Cornelissen, J. J. L. M.; Nolte, R. J. M.; Van Hest, J. C. M. *Small* **2016**, *12*, 2476–2483.

(10) Salgado, E. N.; Radford, R. J.; Tezcan, F. A. *Acc. Chem. Res.* **2010**, *43*, 661–672.

(11) Nepal, M.; Sheedlo, M. J.; Das, C.; Chmielewski, J. *J. Am. Chem. Soc.* **2016**, *138*, 11051–11057.

(12) Kumpfer, J. R.; Rowan, S. J. *ACS Macro Lett.* **2012**, *1*, 882–887.

(13) Michal, B. T.; McKenzie, B. M.; Felder, S. E.; Rowan, S. J. *Macromolecules* **2015**, *48*, 3239–3246.

(14) Mozhdehi, D.; Ayala, S.; Cromwell, O. R.; Guan, Z. *J. Am. Chem. Soc.* **2014**, *136*, 16128–16131.

(15) Grindy, S. C.; Learsch, R.; Mozhdehi, D.; Cheng, J.; Barrett, D. G.; Guan, Z.; Messersmith, P. B.; Holten-Andersen, N. *Nat. Mater.* **2015**, *14*, 1181–1292.

(16) Whittell, G. R.; Hager, M. D.; Schubert, U. S.; Manners, I. *Nat. Mater.* **2011**, *10*, 176–188.

(17) Ott, C.; Hoogenboom, R.; Hoeppener, S.; Wouters, D.; Gohy, J.-F.; Schubert, U. S. *Soft Matter* **2008**, *5*, 84–91.

(18) Gao, H.; Liu, G.; Chen, X.; Hao, Z.; Tong, J.; Lu, L.; Cai, Y.; Long, F.; Zhu, M. *Macromolecules* **2010**, *43*, 6156–6165.

(19) Chen, X.; Xu, N.; Li, N.; Lu, L.; Cai, Y.; Zhao, Y.; Wang, D. *Soft Matter* **2013**, *9*, 1885–894.

(20) Wu, X.; Xu, N.; Zhu, Z.; Cai, Y.; Zhao, Y.; Wang, D. *Polym. Chem.* **2014**, *5*, 1202–1209.

(21) Xu, N.; Han, J.; Zhu, Z.; Song, B.; Lu, X.; Cai, Y. *Soft Matter* **2015**, *11*, 5546–5553.

(22) Wang, Y.; Hollingsworth, A. D.; Yang, S. K.; Patel, S.; Pine, D. J.; Weck, M. *J. Am. Chem. Soc.* **2013**, *135*, 14064–14067.

(23) Lunn, D. J.; Gould, O. E. C.; Whittell, G. R.; Armstrong, D. P.; Mineart, K. P.; Winnik, M. A.; Spontak, R. J.; Pringle, P. G.; Manners, I. *Nat. Commun.* **2016**, *7*, 12371.

(24) Martinez, J. S.; Zhang, G. P.; Holt, P. D.; Jung, H.-T.; Carrano, C. J.; Haygood, M. G.; Butler, A. *Science* **2000**, *287*, 1245–1247.

(25) Butler, A.; Theisen, R. M. *Coord. Chem. Rev.* **2010**, *254*, 288–296.

(26) Chen, C.; Wylie, R. A. L.; Klinger, D.; Connal, L. A. *Chem. Mater.* **2017**, *29*, 1918–1945.

DOI: 10.1021/jacs.7b11005
J. Am. Chem. Soc. 2018, 140, 1409–1414

(27) Roy, D.; Cambre, J. N.; Sumerlin, B. S. *Prog. Polym. Sci.* **2010**, *35*, 278−301.
(28) Stuart, M. A. C.; Huck, W. T. S.; Genzer, J.; Müller, M.; Ober, C.; Stamm, M.; Sukhorukov, G. B.; Szleifer, I.; Tsukruk, V. V.; Urban, M.; Winnik, F.; Zauscher, S.; Luzinov, I.; Minko, S. *Nat. Mater.* **2010**, *9*, 101−113.
(29) Cui, H.; Webber, M. J.; Stupp, S. I. *Biopolymers* **2010**, *94*, 1−18.
(30) Mikhalevich, V.; Craciun, I.; Kyropoulou, M.; Palivan, C. G.; Meier, W. *Biomacromolecules* **2017**, *18*, 3471−3480.
(31) Evers, T. H.; Appelhof, M. A. M.; Meijer, E. W.; Merkx, M. *Protein Eng., Des. Sel.* **2008**, *21*, 529−536.
(32) Valenti, L. E.; De Pauli, C. P.; Giacomelli, C. E. *J. Inorg. Biochem.* **2006**, *100* (2), 192−200.
(33) Velonia, K.; Rowan, A. E.; Nolte, R. J. M. *J. Am. Chem. Soc.* **2002**, *124*, 4224−4225.
(34) Mantovani, G.; Lecolley, F.; Tao, L.; Haddleton, D. M.; Clerx, J.; Cornelissen, J. J. L. M.; Velonia, K. *J. Am. Chem. Soc.* **2005**, *127*, 2966−2973.
(35) Moyer, T. J.; Finbloom, J. A.; Chen, F.; Toft, D. J.; Cryns, V. L.; Stupp, S. I. *J. Am. Chem. Soc.* **2014**, *13*, 14746−14752.
(36) Good, N. E.; Winget, G. D.; Winter, W.; Connolly, T. N.; Izawa, S.; Singh, R. M. M. *Biochemistry* **1966**, *5*, 467−477.
(37) Kodama, M.; Miyata, T. *Thermochim. Acta* **1995**, *267*, 365−372.
(38) Bailey, J. B.; Subramanian, R. H.; Churchfield, L. A.; Tezcan, F. A. *Methods Enzymol.* **2016**, *580*, 223−250.
(39) Salgado, E. N.; Faraone-Mennella, J.; Tezcan, F. A. *J. Am. Chem. Soc.* **2007**, *129*, 13374−13375.
(40) Salgado, E. N.; Lewis, R. A.; Mossin, S.; Rheingold, A. L.; Tezcan, F. A. *Inorg. Chem.* **2009**, *48*, 2726−2728.
(41) Harding, M. M.; Nowicki, M. W.; Walkinshaw, M. D. *Crystallogr. Rev.* **2010**, *16*, 247−302.

DOI: 10.1021/jacs.7b11005
J. Am. Chem. Soc. 2018, 140, 1409−1414

Control of Amphiphile Self-Assembly via Bioinspired Metal Ion Coordination

Abigail S. Knight*[†], Josefin Larsson[†], Jing M. Ren[†], Raghida Bou Zerdan[†], Shay Seguin[†], Remy Vrahas[†], Jianfang Liu[‖], Gang Ren[‖], Craig J. Hawker*[†‡]

[†]California NanoSystems Institute and Materials Research Laboratory and [‡]Materials Department and Department of Chemistry and Biochemistry, University of California, Santa Barbara, California 93106, United States, [‖]The Molecular Foundry, Lawrence Berkeley National Laboratory, Berkeley, CA 94720, United States

aknight@berkeley.edu, hawker@mrl.ucsb.edu

Supporting Information

Table of contents **Page**

Experimental Information

General Information

^{1}H (^{13}C) nuclear magnetic resonance (NMR) spectra were recorded on a Varian VNMRS 600 (150) MHz spectrometer. Chemical shifts (δ) are reported in ppm relative to residual chloroform in $CDCl_3$ (7.26 ppm). Size exclusion chromatography (SEC) was conducted on a Waters 2695 separation module using 0.25% trimethylamine/chloroform as the mobile phase equipped with a Waters 2414 refractive index detector. Number-average molar mass (M_n) and mass-average molar mass (M_w) were determined relative to linear polystyrene standards and used to estimate the molar mass dispersity ($Đ = M_M/M_n$). MALDI-TOF mass spectra were obtained with a Bruker microflex LRF. MALDI samples (2 µL) were mixed with matrix solution (2 µL, 5 mg α-cyano-4-hydroxycinnamic acid in 1:1 water:acetonitrile with 0.1% trifluoroacetic acid and 6 mM ammonium phosphate to suppress matrix ionization[1]) and spotted directly on a stainless steel sample plate. Thermal gravimetric analysis (TGA) was performed using a TA Discovery TGA at a heating rate of 10 °C/min using 3–5 mg of sample in an alumina sample cup atop a platinum or ceramic hanging pan (under nitrogen). The data were analyzed using Trios software V3.3. Differential scanning calorimetry (DSC) was conducted on a PerkinElmer DSC 8000 outfitted with a liquid nitrogen cooling module at a heating/cooling rate of 35 °C/min using 3–5 mg of sample in a hermetically sealed aluminum pan, with respect to an empty reference pan. Three cycles of heating and subsequent cooling were performed through the desired temperature range. The FTIR spectra were collected on a Nicolet is10 FTIR equipped with a Smart Diamond ATR accessory, working in the mid infrared range of 4,000 to 500 cm^{-1}.

All chemicals were used as obtained unless otherwise specified. Bicyclo[2.2.1]hept-5-ene-2,3-dicarboxylic anhydride (>95%), ethanolamine (>99%), *N*,*N*′,*N*″,*N*‴-pentamethyldiethylenetriamine, and styrene (containing 4-*tert*-butylcatechol as stabilizer, ≥99%) were purchased from Sigma Aldrich and triethylamine (98%) was purchased from Fisher Scientific. All doubly distilled water (ddH_2O) was obtained from a MilliQ water purification system. The hexahistidine-cysteine peptide was supplied by New England Peptides (>95%). *N*-2-hydroxyethylpiperazine-*N*-2-ethane sulfonic acid (HEPES) was purchased as a 1 M solution (pH 7) from Life Technologies and diluted with ddH_2O for all assays. Nickel(II) chloride hexahydrate, cobalt(II) nitrate hexahydrate, copper(II) chloride hexahydrate, copper(I) bromide, manganese(II) chloride tetrahydrate, zinc(II) chloride, and iron(II) chloride tetrahydrate were purchased from Sigma Aldrich (≥99.995% trace metals basis). Additional metal salts used include magnesium chloride (Sigma Aldrich, >98%), zinc acetate (Sigma Aldrich, 99.99%), zinc nitrate hexahydrate (Sigma Aldrich, 99.999%), and cadmium nitrate tetrahydrate (Acros, >99%).

Synthesis of furan-protected maleimide initiator for copper-catalyzed ATRP

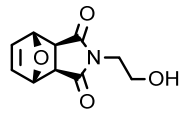

(3aR,4S,7R,7aS)-2-(2-hydroxyethyl)-3a,4,7,7a-tetrahydro-1H-4,7-epoxyisoindole-1,3(2H)-dione:
Bicyclo[2.2.1]hept-5-ene-2,3-dicarboxylic anhydride (1.00 g, 6.02 mmol) was suspended in MeOH (25 mL) and the mixture was cooled to 0 °C. Ethanolamine (0.55 mL, 6.02 mmol) was added dropwise over 10 min, and the resulting solution was stirred for 5 min at 0 °C, then 30 min at ambient temperature, and finally refluxed for 4 h. After cooling the mixture to ambient temperature, the solvent was removed under reduced pressure, and the white residue was dissolved in 100 mL of CH_2Cl_2 and washed with 3 × 100 mL of water. The organic layer was dried over $MgSO_4$, filtered, and concentrated under reduced pressure to afford the crude product as an off-white residue, which was purified by flash chromatography on silica gel in 100% ethyl acetate to give the product as a white powder (0.66 g, 52%). IR (cm^{-1}) ν_{max} 3474 (OH), 1684 (*C*=*O*)N; ^{1}H NMR (600 MHz, $CDCl_3$): δ 6.53 (t, J = 1.0 Hz, 2H), 5.29 (t, J = 1.0 Hz, 2H), 3.78 – 3.77 (m, 2H), 3.72 – 3.70 (m, 2H), 2.89 (s, 2H), 2.14 (s, 1H); ^{13}C NMR (150 MHz, $CDCl_3$): δ 176.8, 136.6, 81.0, 60.0, 47.5, 41.7; HRMS (ESI) (m/z): calcd for $C_{10}H_{11}NO_4$ $[M + Na]^+$: 232.0586, found: 232.0557.

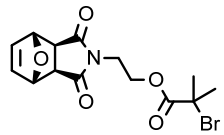

2-((3aR,4S,7R,7aS)-1,3-dioxo-1,3,3a,4,7,7a-hexahydro-2H-4,7-epoxyisoindol-2-yl)ethyl 2-bromo-2-methylpropanoate: A suspension of the alcohol ((3a*R*,4*S*,7*R*,7a*S*)-2-(2-hydroxyethyl)-3a,4,7,7a-tetrahydro-1*H*-4,7-epoxyisoindole-1,3(2*H*)-dione, 0.50 g, 2.4 mmol) and Et_3N (0.24 mL, 2.6 mmol) in anhydrous THF (25 mL) was cooled to 0 °C, then a solution of 2-bromo isobutyryl bromide (0.33 mL, 2.6 mmol) in 8 mL of THF was added dropwise over 30 min. The white suspension was stirred for 3 h at 0 °C and subsequently at ambient temperature overnight. The ammonium salt was filtered off and the solvent removed under reduced pressure to give a pale yellow residue that was purified by flash chromatography on silica gel in 1:1 mixture of petroleum ether/ethyl acetate to afford the pure product as a white powder (0.82 g, 96%). IR (cm^{-1}) ν_{max} 1733 (*C*=*O*)O, 1694 (*C*=*O*)N; ^{1}H NMR (600 MHz, $CDCl_3$): δ 6.51 (t, J = 0.9 Hz, 2H), 5.26 (t, J = 0.8 Hz, 2H), 4.34 – 4.31 (m, 2H), 3.83 – 3.80 (m, 2H), 2.87 (s, 2H), 1.89 (s, 6H); ^{13}C NMR (150 MHz, $CDCl_3$): δ 175.9, 171.4, 136.6, 80.9, 62.2, 55.8, 47.5, 37.6, 30.6; HRMS (ESI) (m/z): calcd for $C_{14}H_{16}BrNO_5$ $[M + Na]^+$: 380.0110, found: 380.0053.

Maleimide-oligostyrene synthesis and purification

Due to limited solubility of the initiator in styrene, a stock solution of the furan-protected maleimide ATRP initiator was first made (toluene, 90 mM) and degassed. *N*,*N*,*N*′,*N*″,*N*″-Pentamethyldiethylenetriamine (PMDETA) and styrene, filtered through basic alumina, were degassed in separate vials before use. A vial was charged with CuBr (35 mg, 0.24 mmol, 0.5 eq), $CuBr_2$ (21 mg, 0.096 mmol, 0.2 eq), and a stir bar and purged with Ar for 10 min. Degassed styrene (5.0 g, 48 mmol, 100 eq) and PMDETA (42 mg, 0.24 mmol, 0.5 eq) were then injected via syringe under Ar to the vial and allowed to stir at r.t. until the solution turned green, indicating copper complex formation. The initiator solution was then added via syringe (172 mg, 0.48 mmol, 1 eq) and the reaction mixture was stirred in an oil bath at 80 °C. Aliquots (1 mL) were quenched at 15-minute time intervals by flash freezing in liquid N_2 and exposing the frozen reaction mixture to air as it thawed. After reaching room temperature, the mixtures were filtered through basic alumina using hexane to elute unreacted monomer and ethyl acetate to elute the oligomer. The oligomer was collected and dried under reduced pressure to give the furan protected maleimide oligostyrene. A 1 mL aliquot from a reaction time of 45 min (approx.. 10% conversion, $M_{n,\,NMR}$ = 930, 48 mg) was used for further reactions. ^{1}H NMR (600 MHz, $CDCl_3$): δ 7.35-6.32 (aromatic), 6.52-6.45 (2H), 5.52 (2H), 4.62-4.37 (1H), 3.74-3.30 (4H), 2.59-0.71 (backbone); ^{13}C NMR (100 MHz, $CDCl_3$): δ 177.0, 175.8, 145.3, 136.6, 128.6, 128.5, 118.2, 128.1, 128.0, 127.8, 127.6, 126.4, 125.9, 80.9, 60.4, 57.3, 55.9, 47.5, 42.8, 41.6, 40.8, 40.4, 40.0, 39.8, 37.7

To deprotect the chain end, the oligomer was re-dissolved in toluene (2 mL) and refluxed at 120 °C overnight. The maleimide-terminated oligostyrene was isolated by removing the solvent under reduced pressure and stored at −20 °C (^{1}H-NMR spectrum and SEC trace Figure S3). ^{1}H NMR (600 MHz, $CDCl_3$): δ 7.35-6.32 (aromatic), 4.62-4.37 (1H), 3.74-3.30 (4H), 2.59-0.71 (backbone)

Amphiphile (oSt(His)$_6$) synthesis and purification

Note: Preliminary characterization of conjugation and self-assembly were performed from batches produced with 0.1 mg and 1 mg of peptide. However, materials used in all reported self-assembly characterization originated from a single 5 mg scale reaction performed to limit any variation.

DMF was bubbled with Ar to degas before use to avoid dimerization of the amphiphiles via disulfide formation. A stock solution of maleimide-oligostyrene (100 mg/mL, 120 mM in DMF) stored at −20 °C for up to six months was used for all reactions. Peptides were dissolved in 10 eq (relative to the peptide) of HEPES buffer (pH 7) and lyophilized to buffer any residual trifluoroacetic acid from the peptide synthesis and ensure a neutral pH. The lyophilized $(His)_6$Cys peptide was dissolved in DMF (5 mg, 5.3 µmol) and combined with 155 µL of oligostyrene (3 eq) and incubated at room temperature for 1 h. The reaction mixture was stopped by diluting the mixture with 0.1% trifluoroacetic acid (TFA, Millipore) in ddH_2O (2.25 mL). The crude mixture was divided into five equal volume fractions for purification with Sep-Pak cartridges (C18 1 cc Vac Cartridge, 50 mg Sorbent per Cartridge, Millipore). All solvents used in the purification contain 0.1% TFA. A schematic of this purification is provided in Figure S4b. The columns were swelled with three column volumes of acetonitrile and equilibrated with ddH_2O (3 mL) before loading the sample. ddH_2O (3 mL) was used to rinse the residual DMF and buffer salts from the reaction mixture off the column. Acetonitrile : ddH_2O 1:3 (3 mL)

was used to elute remaining peptide and the amphiphile product, respectively. The amphiphile was then dried under reduced pressure, re-suspended in ddH_2O, and freeze dried. The freeze-dried amphiphile was then re-dissolved in ddH_2O, and filtered through a 0.22 μm centrifugal filter (Ultrafree-MC GV centrifugal filter, Millipore) to remove any insoluble aggregates. The amphiphile was freeze-dried again to determine the weight of the remaining material (typical yields ~50%) and then redissolved in ddH_2O, separated into 0.5 mg aliquots, and stored dry at −20 °C. Stock solutions of the amphiphiles were made (6 mM in ddH_2O) for characterization and could be stored at −20 °C for up to 2 months before any observable degradation.

Critical aggregation concentration characterization

Samples of oSt$(His)_6$ at concentrations of 0.3 μM to 600 μM were incubated at r.t. with Nile Red (70 nM) in HEPES (100 mM, pH 7) for 1 h and the fluorescence was measured with a Tecan M220 Plate Reader.

General procedure for self-assembly

Assembly solutions contained volumes from 10 μL to 50 μL oSt$(His)_6$ (600 μM), 100 mM HEPES (pH 7), and 15 mM metal salt unless otherwise noted. The self-assembly samples were prepared in PCR tubes (Bio-Rad Laboratories), heated in a Biometra T3000 thermocycler to 80 °C for 30 min (unless otherwise noted), and allowed to slowly cool down to r.t. overnight. **Note:** heating in the thermocycler prevents condensation of the water on the lid of the PCR tube used for these small volume assemblies.

Dynamic light scattering (DLS)

Assembled samples of oSt$(His)_6$ (600 μM) were diluted 11-fold (5 μL sample into 50 μL buffer) into HEPES (pH 7, 100 mM) unless otherwise noted. The samples weretransferred to disposable ultra-microcuvettes (BrandTech Scienctific, Inc), and analyzed with a Malvern Zetasizer Nano ZS. The number-average particle size distribution was recorded for each of the samples.

Preparation and imaging of negative-stained TEM samples

All samples were used directly from the assembly reaction mixture (oSt$(His)_6$ (600 μM), HEPES buffer (pH 7, 100 mM)) unless otherwise noted. Negative staining was completed using a procedure adapted from the literature.[2] The TEM grids were glow discharged (15 mA, 20 sec), exposed to 3 μL of the sample (20 sec) followed by two water droplets and two droplets of uranyl formate stain (1 mg/mL, 3 sec and 40 sec exposures, respectively), and then dried overnight. Samples were imaged on an FEI Tecnai G2 Sphera Microscope with an accelerating voltage of 200 kV.

Cryo-electron microscopy (cryo-EM) sample preparation and imaging

The Cryo-EM samples were prepared by the plunge-freezing method. In brief, an aliquot (4 μl) of sample of oSt$(His)_6$ (600 μM or 120 μM) in HEPES buffer was placed on a glow-discharged lacey carbon film grid (Cu-200LC, EMS, Hatfield, PA, USA, and Cu-200LN, Pacific Grid-Tech, San Francisco, USA). The sample grid was blotted with filter paper from one side for 3.5 seconds under 90% humidity at 4 °C using a Leica EM GP rapid-plunging device (Leica, Buffalo Grove, IL, USA), and then flash-frozen in liquid ethane before transferring to liquid nitrogen for storage.

The cryo-EM grid was mounted on a Gatan 915 cryo-holder (Gatan Inc., Pleasanton, CA, USA) and examined by a Zeiss Libra 120 transmission electron microscope (Carl Zeiss SMT GmbH, Oberkochen, Germany) equipped with a LaB6 filament (operating at 120 kV) and 20 eV in-column Ω energy filter. The micrographs were acquired by a 4 k × 4 k Gatan UltraScan 4000 CCD camera at the magnifications of 20 K (5.9 Å/pixel) and 50 K (2.4 Å/pixel) under a dose of ~15 e/Å^2 with defocus of 0.2 - 2 μm. The defocus of each micrograph was examined by EMAN *ctfit* software after the X-ray speckles were removed.[3] The micrographs were filtered by Gaussian boundary low-pass and high-pass filters.

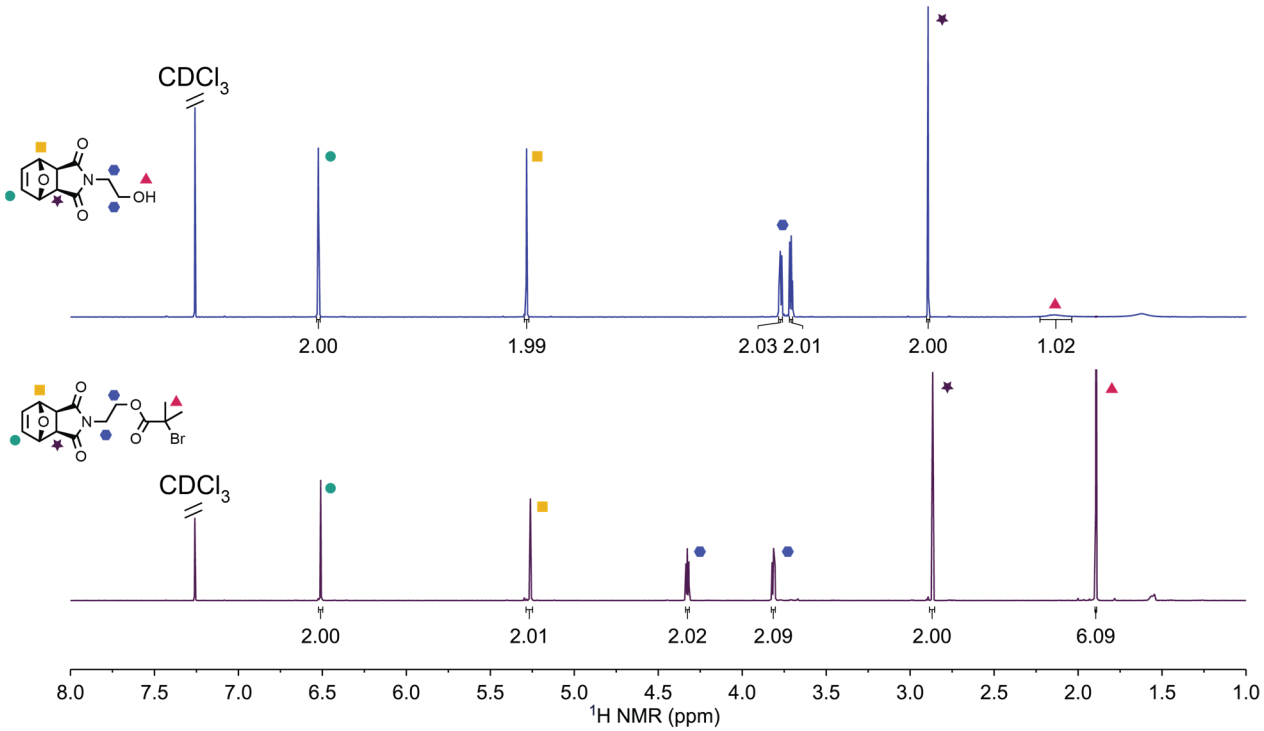

Figure S1. ^{1}H NMR spectra of the furan-protected maleimide initiator and its precursor in $CDCl_3$

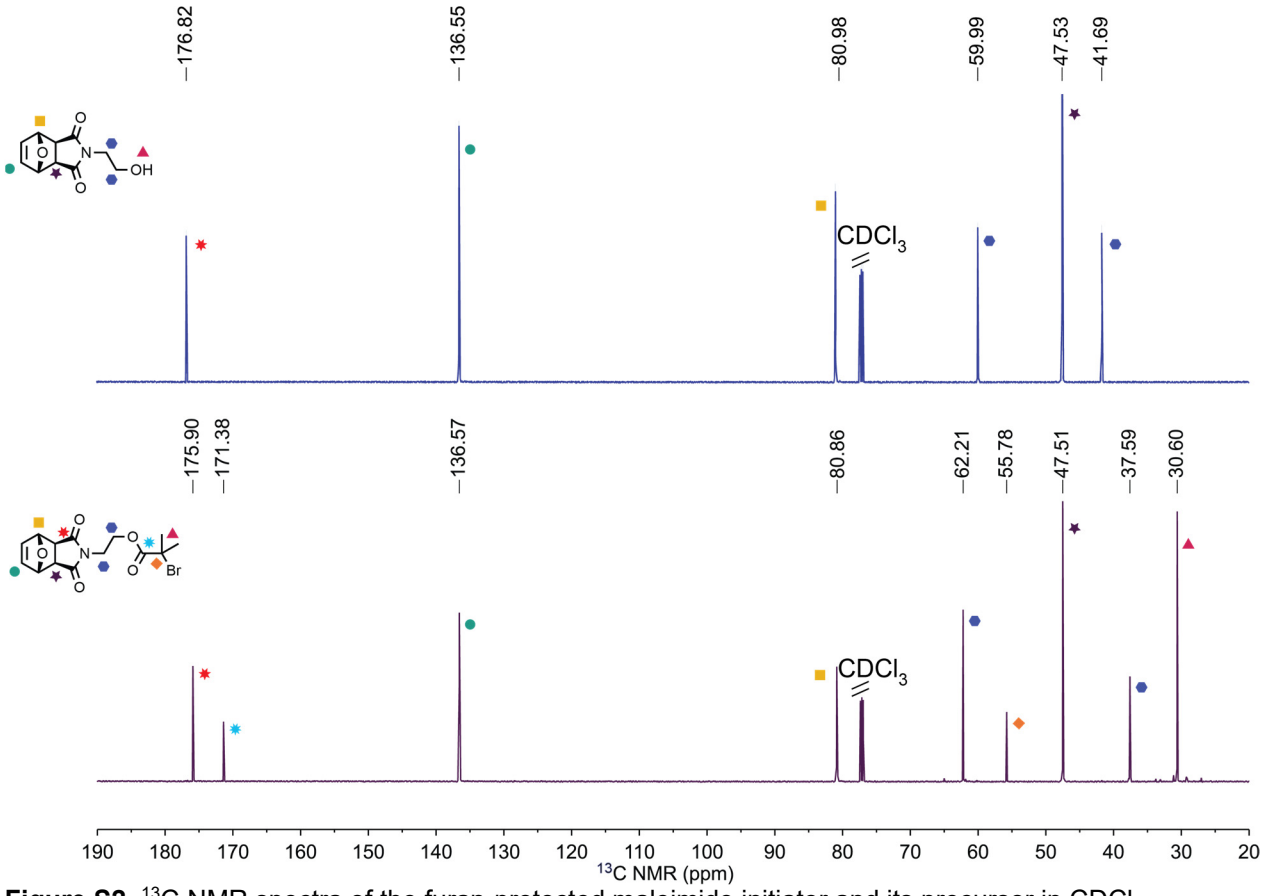

Figure S2. ^{13}C NMR spectra of the furan-protected maleimide initiator and its precursor in $CDCl_3$

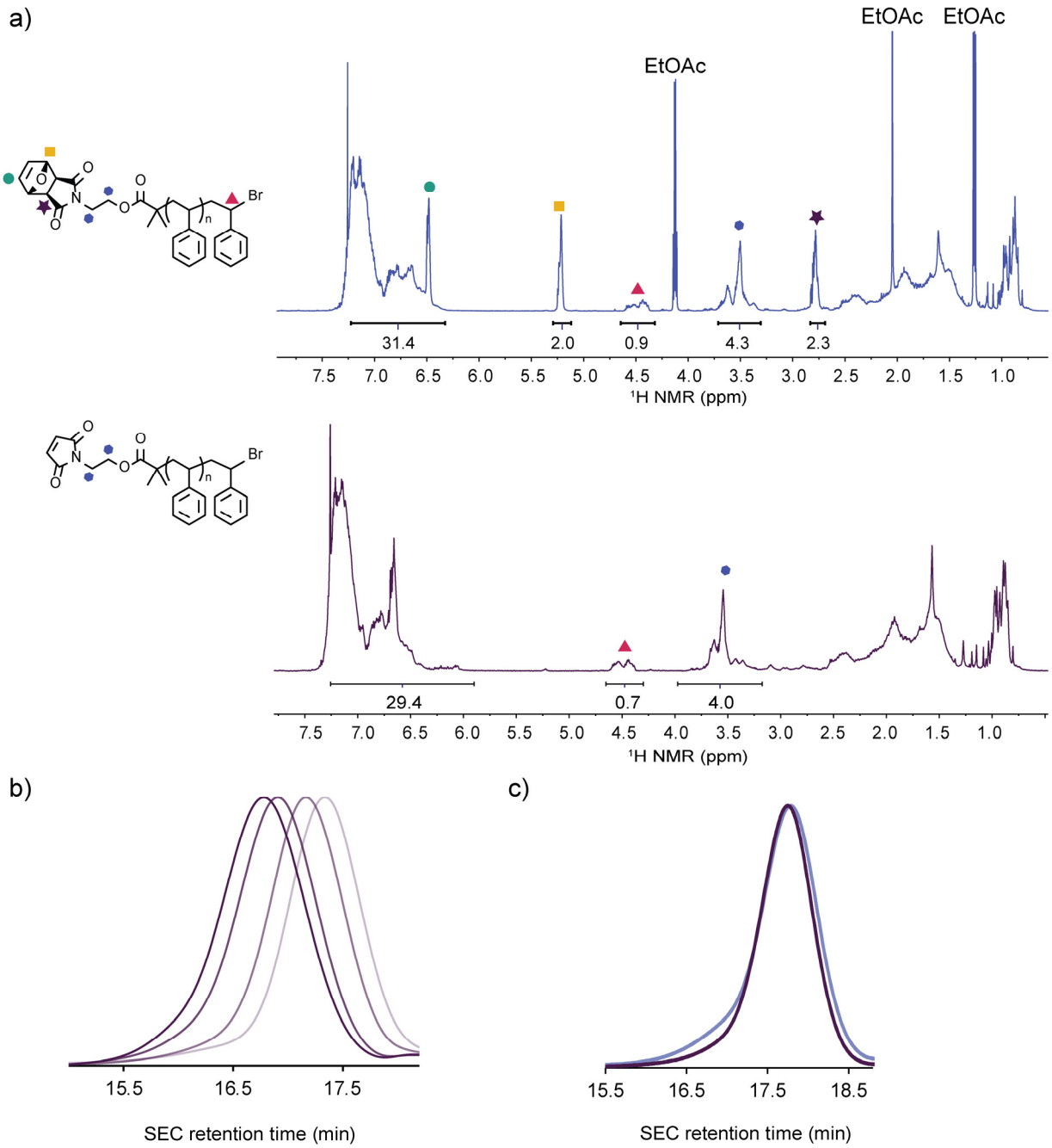

Figure S3. Representative characterization of maleimide-oligostyrene. a) ^{1}H NMR spectra of the furan-protected oligomer and the deprotected oligomer. b) SEC dRI chromatograms monitoring the molecular weight evolution (M_n = 630-1200) of the polymerization. c) SEC dRI chromatogram before (purple) and after (blue) furan deprotection to reveal the maleimide chain end.

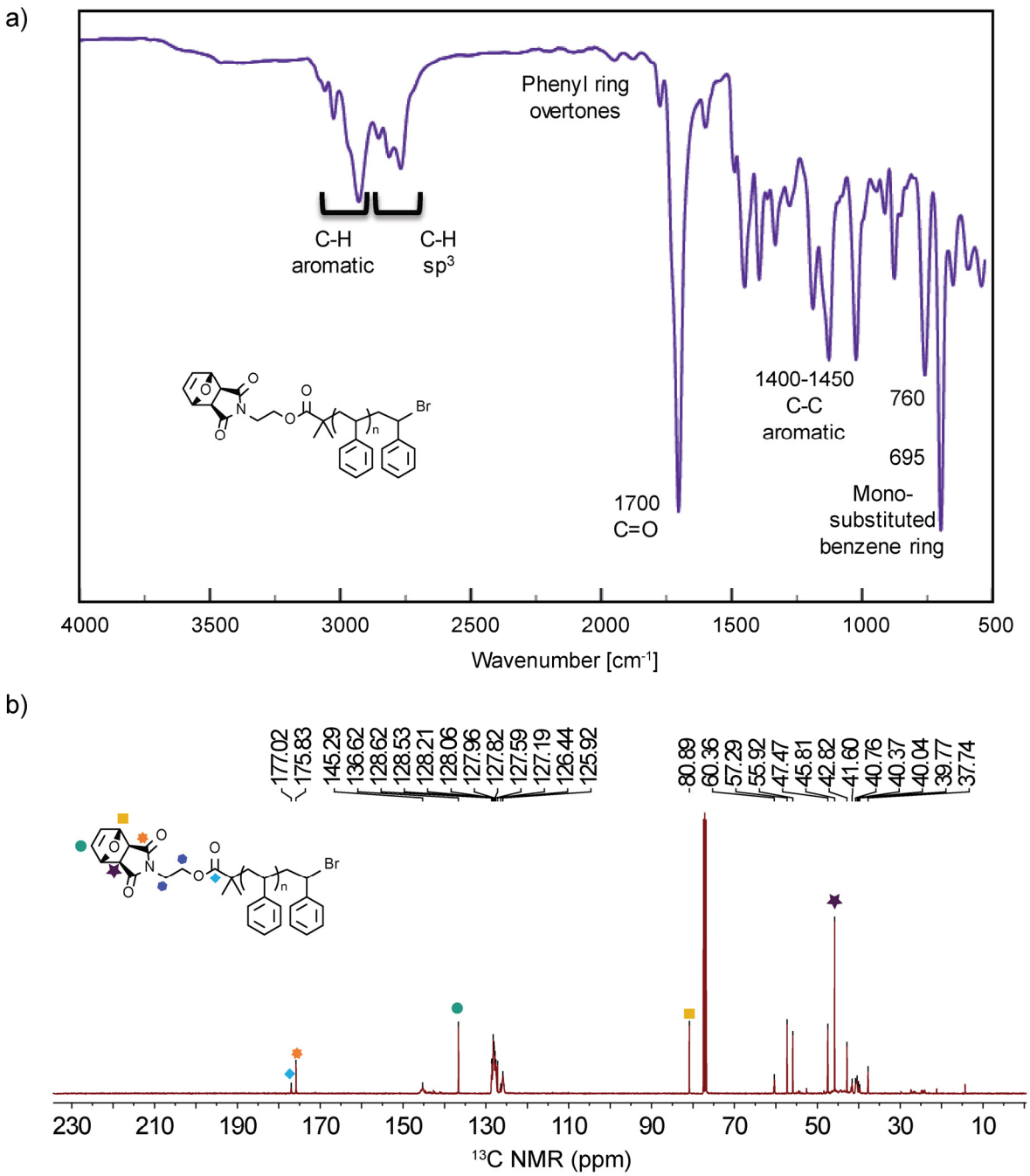

Figure S4. a) IR spectrum of the furan-protected maleimide oligostyrene b) ^{13}C NMR spectrum of the furan-protected maleimide oligostyrene in $CDCl_3$

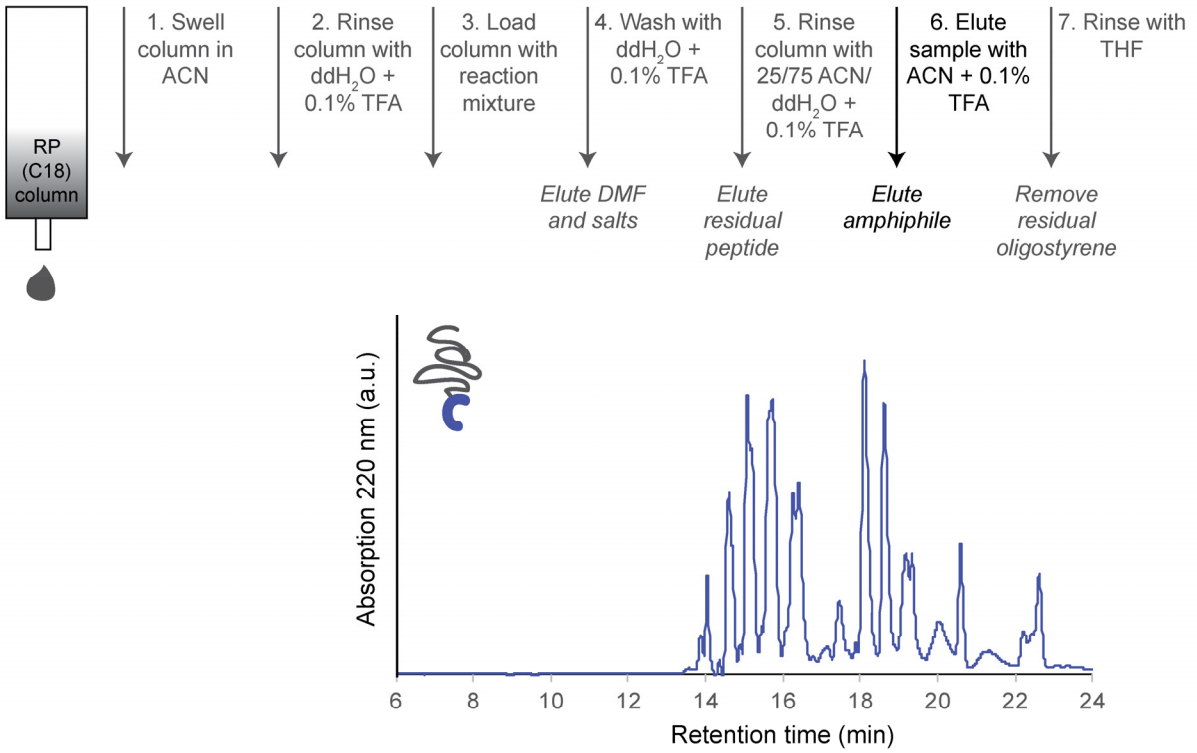

Figure S5. Schematic of the purification of oSt(His)$_6$ with a C18 sep-pak column and HPLC UV chromatogram of the purified product.

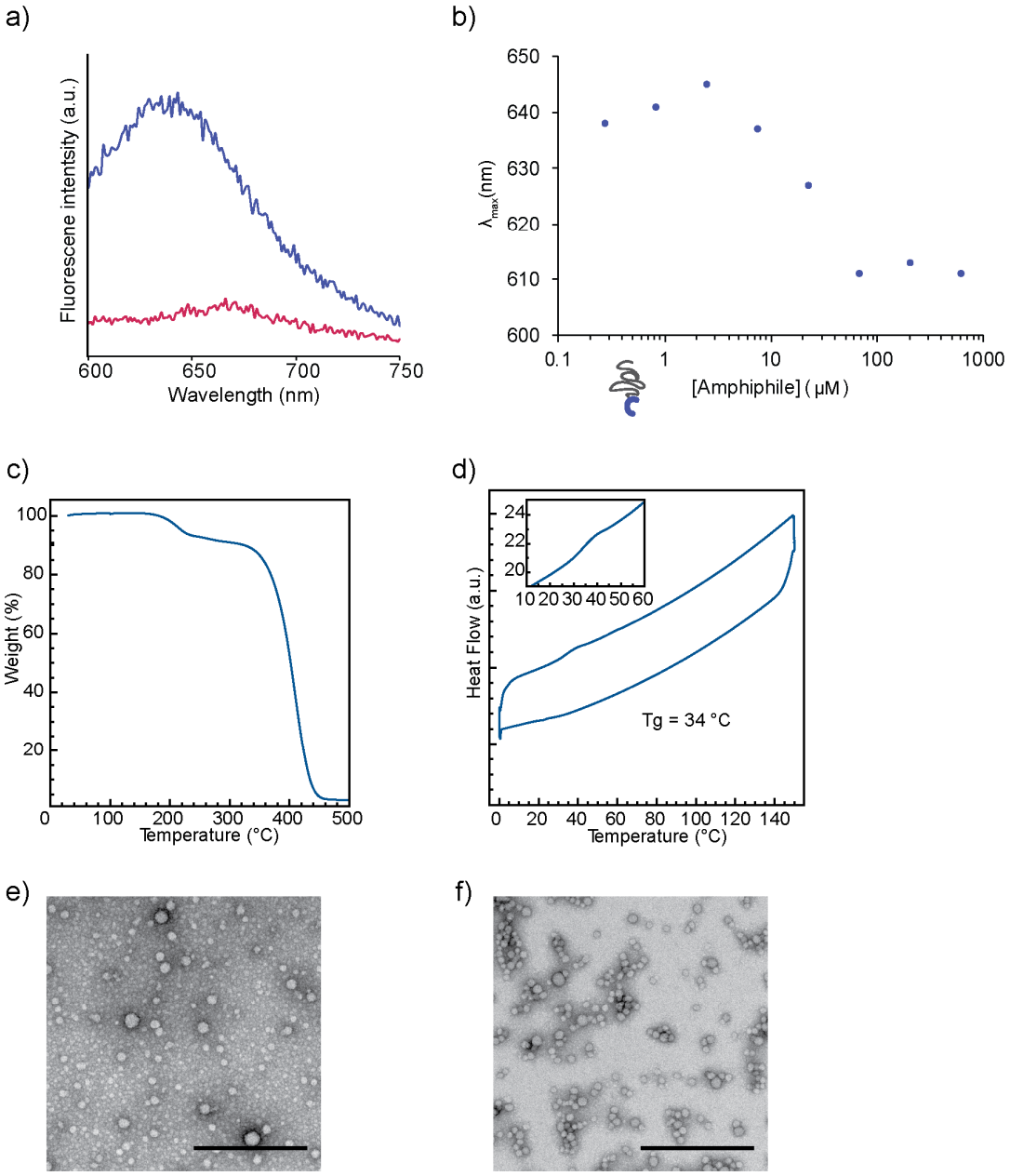

Figure S6. Characterization of assembly parameters for oSt(His)$_6$ a) Calculation of critical aggregation concentration (CAC). Fluorescence spectra for samples containing 0.3 μM (pink) and 600 μM (blue) oSt(His)$_6$ below and above the CAC, respectively. b) The λ_{max} of the fluorescence spectrum for each concentration of oSt(His)$_6$ (0.3 μM to 600 μM) is plotted. All samples were prepared in 100 mM HEPES, pH 7, with 70 nM Nile Red. c) TGA thermogram for the protected maleimide-oligostyrene determined at a heating rate of 10 °C/min under nitrogen d) Differential scanning calorimetry of the oligostyrene showing the glass transition determined at a heating rate of 35 °C/min under nitrogen (Endo Up). Negative stained (uranyl formate) TEM images of oSt(His)$_6$ (600 μM) assembled in the absence (e) and presence (f) of Zn(II) (15 mM) in HEPES (100 mM, pH 7) at room temperature. All scale bars represent 200 nm.

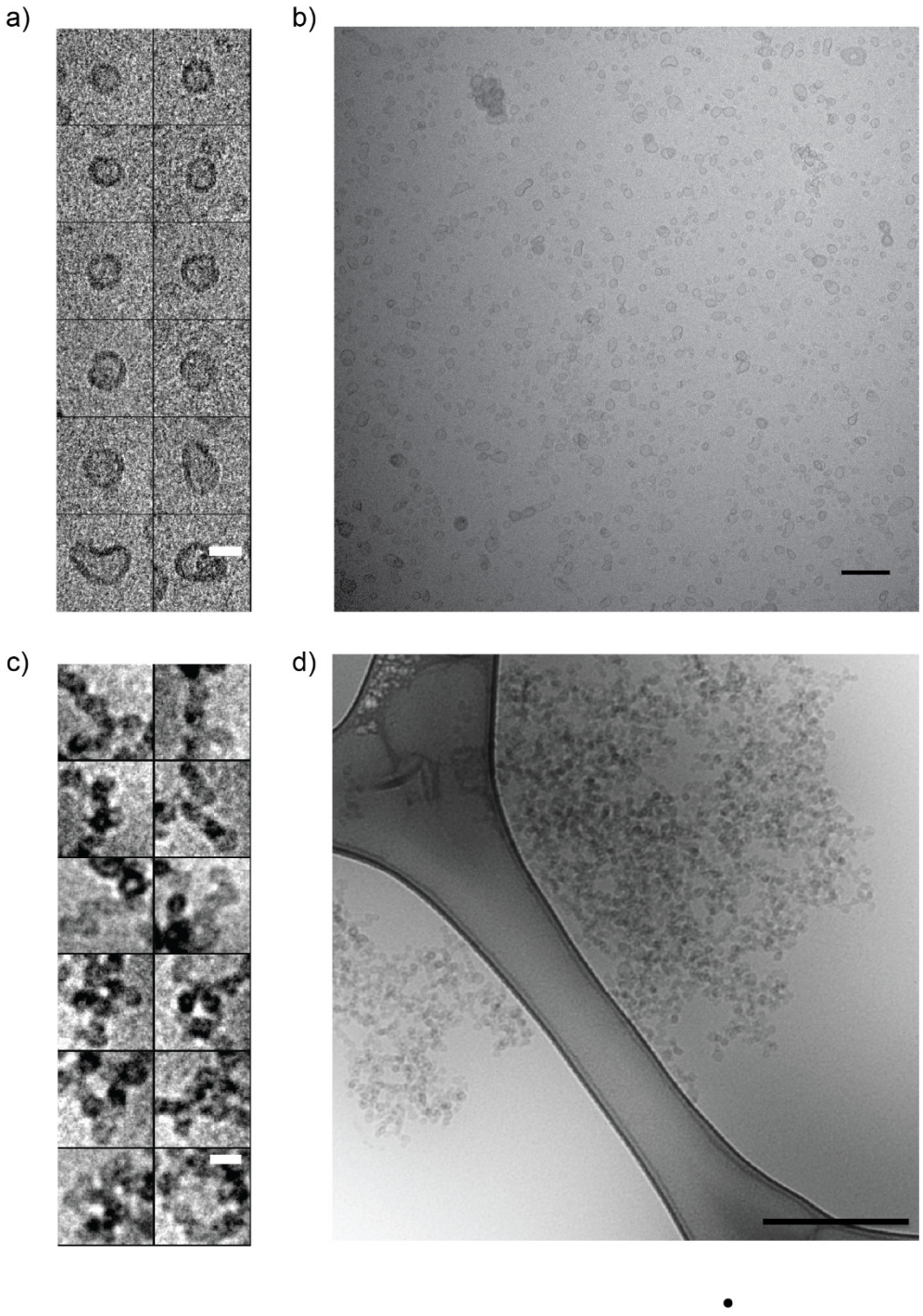

Figure S7. Cryogenic TEM images of samples assembled with no divalent ions a) and b) and Zn(II) (15 mM, c) and d)). Both samples were assembled with oSt(His)$_6$ (600 μM in 100 mM HEPES). Scale bars in a) and c) represent 20 nm and scale bars in b) and d) represent 200 nm.

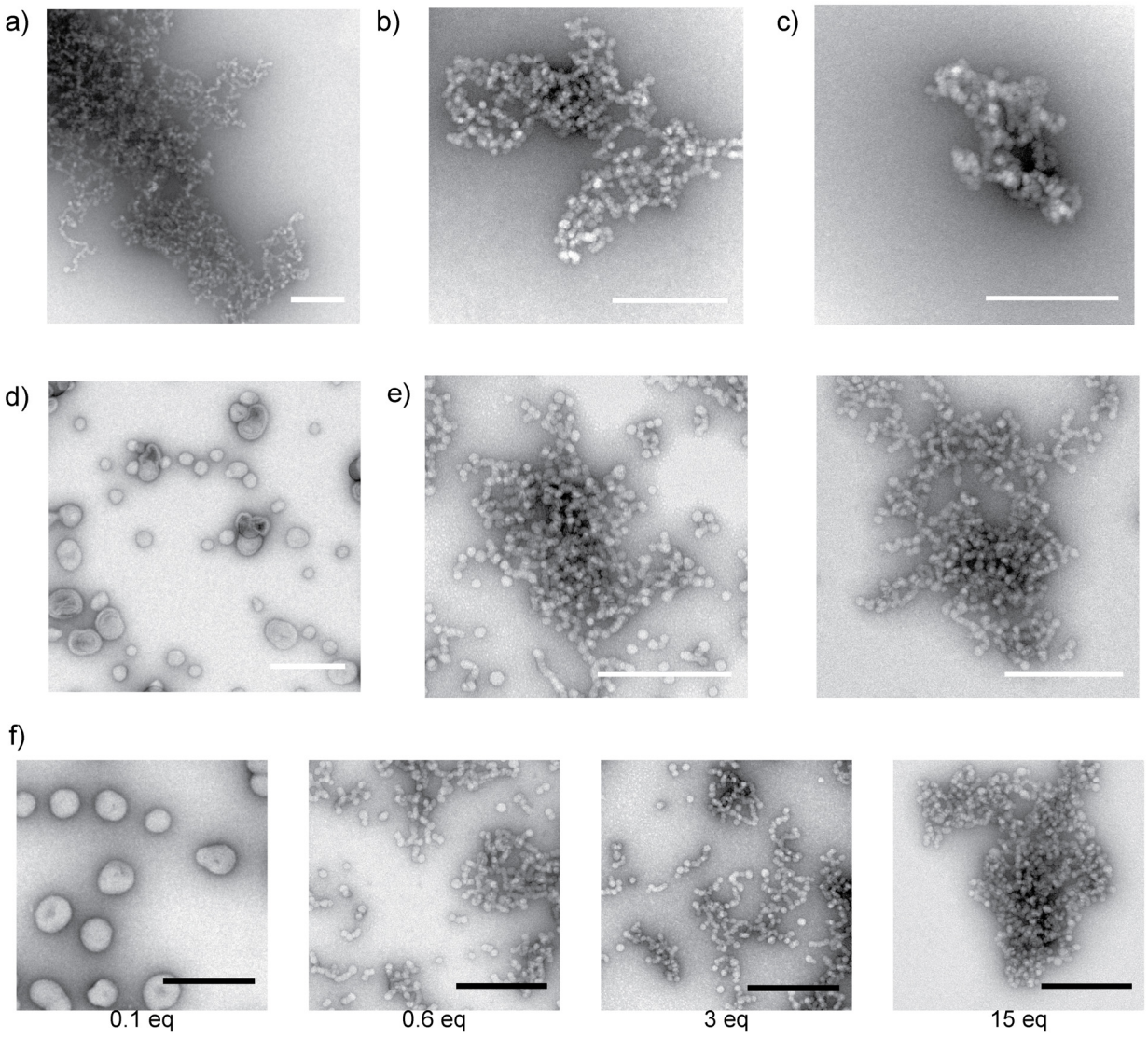

Figure S8. Negative-stained TEM images of control samples. All samples were assembled with 100 mM HEPES, 600 μM oSt(His)$_6$, and 15 mM salt with a divalent cation unless otherwise noted. a) A sample containing $ZnCl_2$ was heated at 80 °C for 30 min, slow cooled in the heat block overnight, and then the process was repeated. b) A sample with $ZnCl_2$ was diluted 10-fold after assembly in ddH_2O. c) d) oSt(His)$_6$ assembled with $MgCl_2$ in PIPES (100 mM, pH 7) instead of HEPES buffer. d) oSt(His)$_6$ assembled with $MgCl_2$. e) Samples assembled with different Zn(II) salts: zinc acetate (left) and zinc nitrate (right). f) Varying concentrations of $ZnCl_2$ (0.1 eq/60 μM, 0.6 eq/360 μM, 3 eq/1.8 mM, 15 eq/9 mM) leading to different degrees of aggregation. All samples negative stained and all scale bars represent 200 nm.

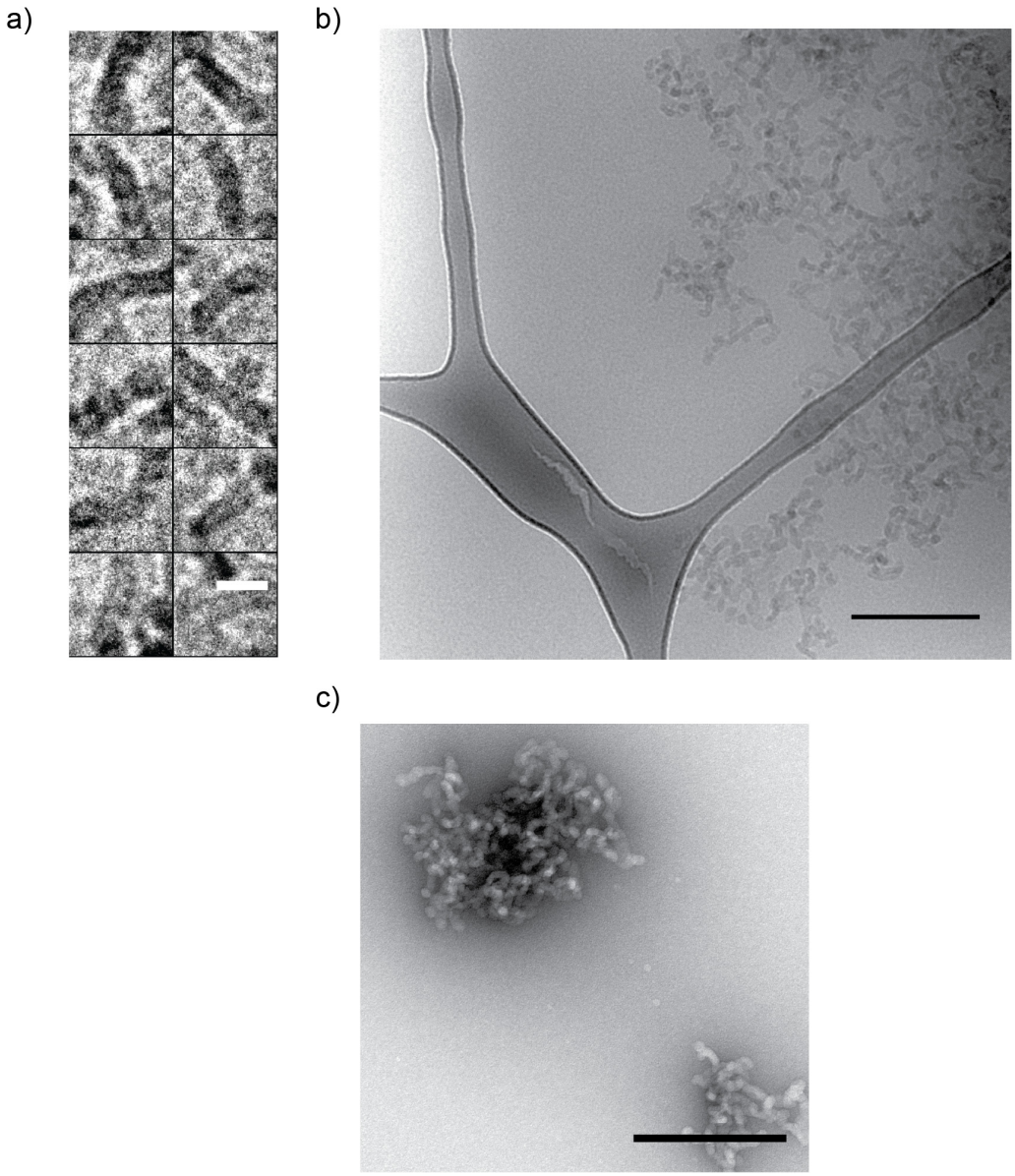

Figure S9. TEM images of oSt(His)$_6$ (600 μM in 100 mM HEPES, pH 7) assemblies in the presence of Co(II) (15 mM). a) Cryogenic image with scale bar representing 20 nm. b) Cryogenic image with scale bar representing 200 nm. c) Negative stained sample with scale bar representing 200 nm.

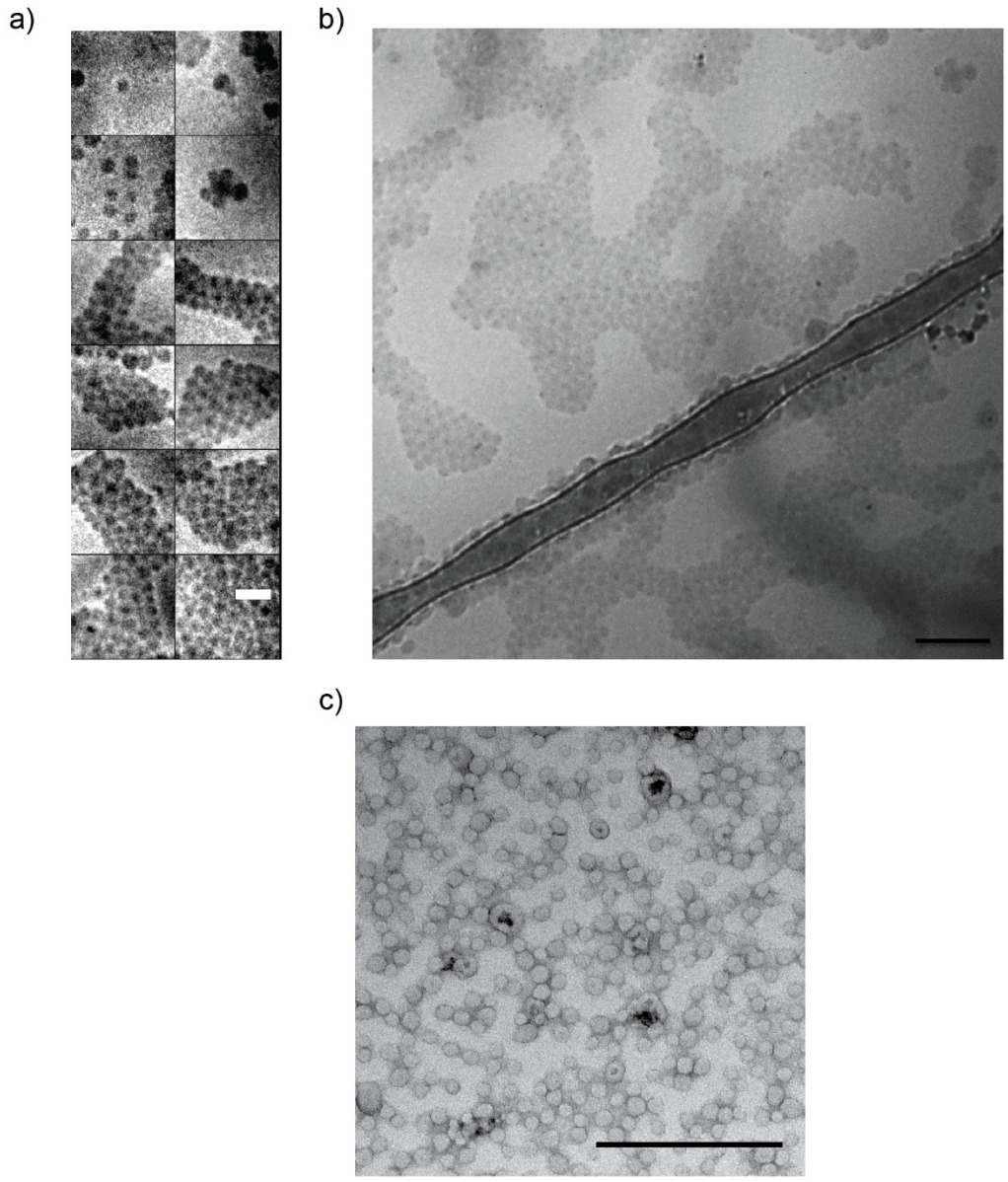

Figure S10. TEM images of oSt(His)$_6$ (600 μM in 100 mM HEPES, pH 7) assemblies in the presence of Cu(II) (15 mM). a) Cryogenic image with scale bar representing 20 nm. b) Cryogenic image with scale bar representing 200 nm. c) Negative stained sample with scale bar representing 200 nm.

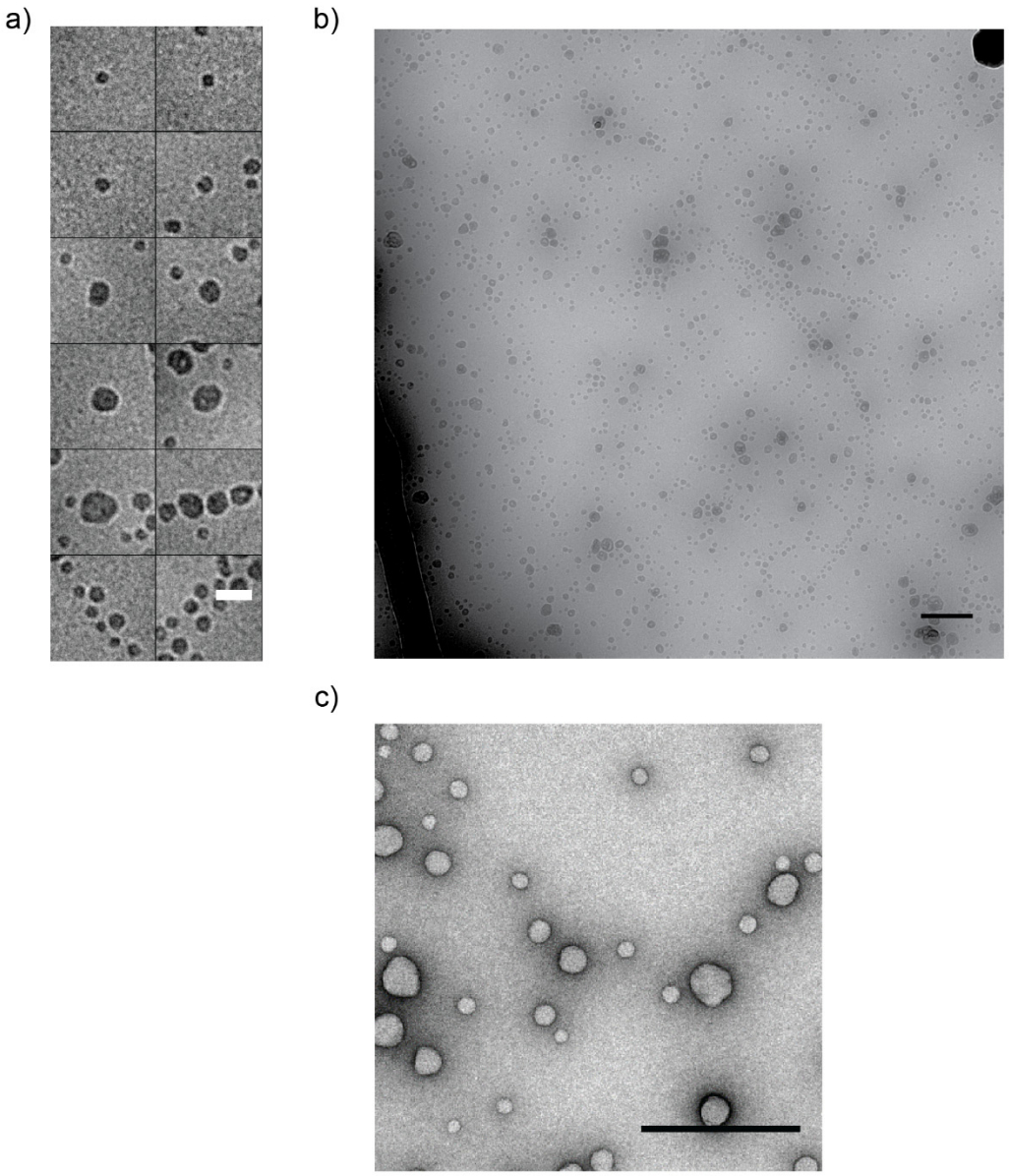

Figure S11. TEM images of oSt(His)$_6$ (600 μM in 100 mM HEPES, pH 7) assemblies in the presence of Ni(II) (15 mM). a) Cryogenic image with scale bar representing 20 nm. b) Cryogenic image with scale bar representing 200 nm. c) Negative stained sample with scale bar representing 200 nm.

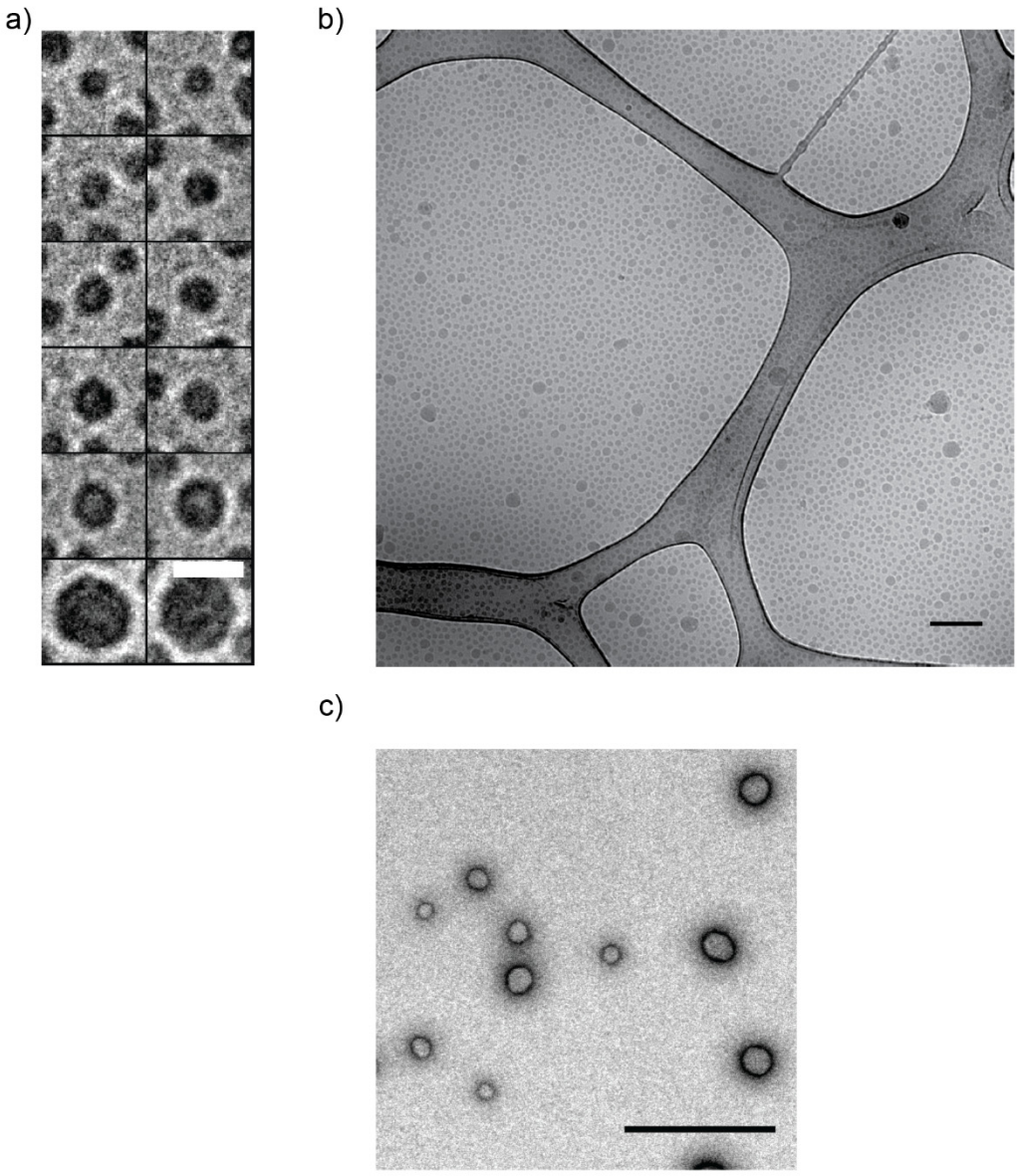

Figure S12. TEM images of oSt(His)$_6$ (600 μM in 100 mM HEPES, pH 7) assemblies in the presence of Cd(II) (15 mM). a) Cryogenic image with scale bar representing 20 nm. b) Cryogenic image with scale bar representing 200 nm. c) Negative stained sample with scale bar representing 200 nm.

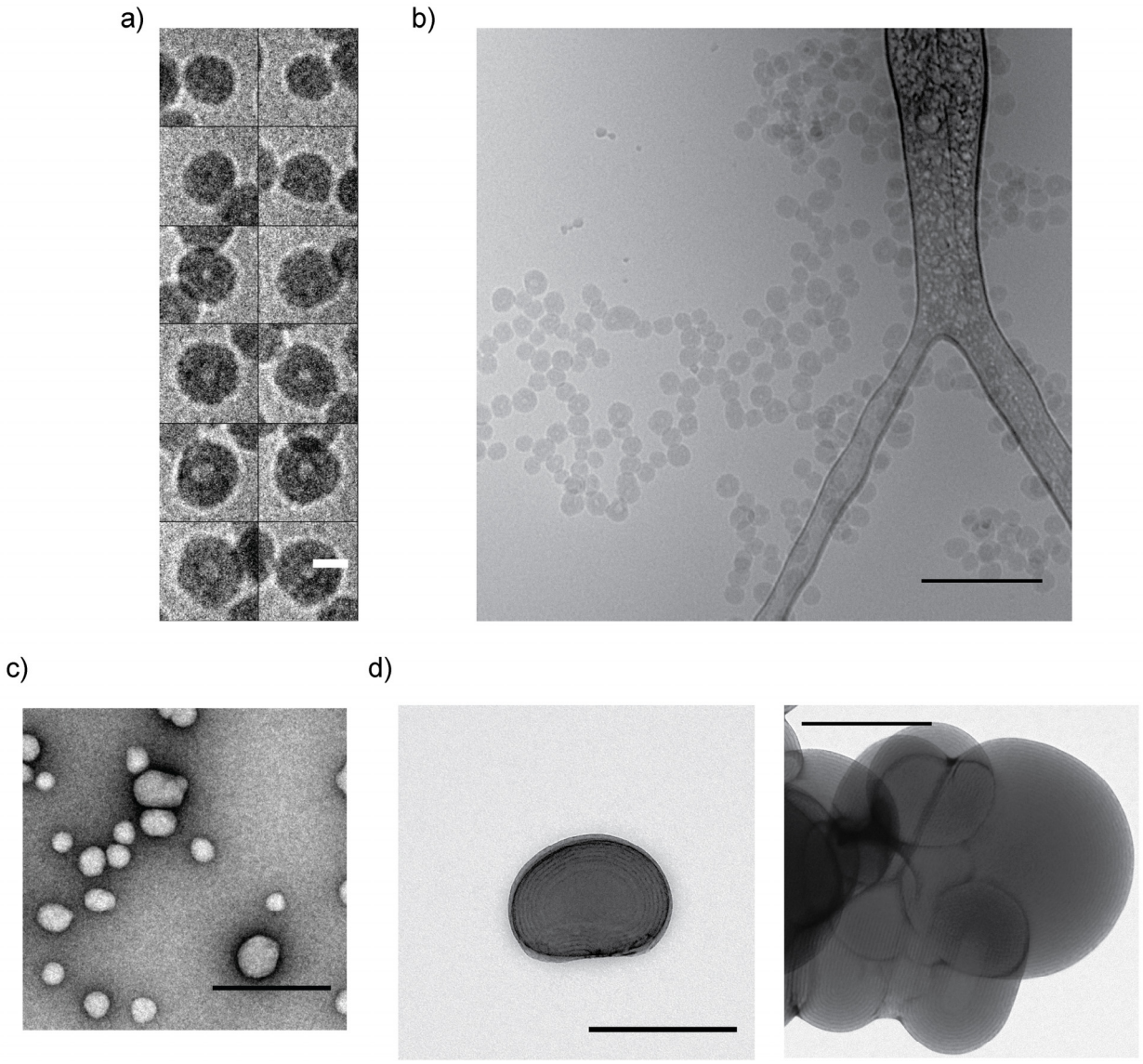

Figure S13. TEM images of oSt(His)$_6$ (600 μM in 100 mM HEPES, pH 7) assemblies in the presence of Mn(II) (15 mM). a) Cryogenic image with scale bar representing 20 nm. b) Cryogenic image with scale bar representing 200 nm. c) Negative stained sample with scale bar representing 200 nm. d) Negative stained images of oSt(His)$_6$ assembled in PIPES buffer (100 mM, pH 7) instead of HEPES buffer. The scale bar represents 200 nm.

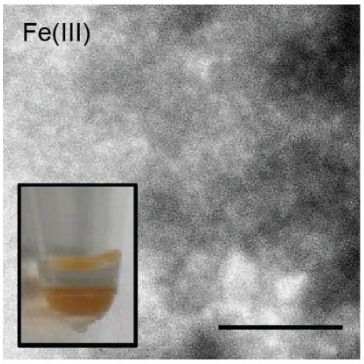

Figure S14. Photograph and TEM image of negative-stained sample of aggregated oSt(His)$_6$ in the presence of Fe(III) (15 mM). Scale bar represents 200 nm. b) DLS number-average particle size distribution of the particles and particle aggregates formed in the presence of the listed ions (15 mM divalent ion).

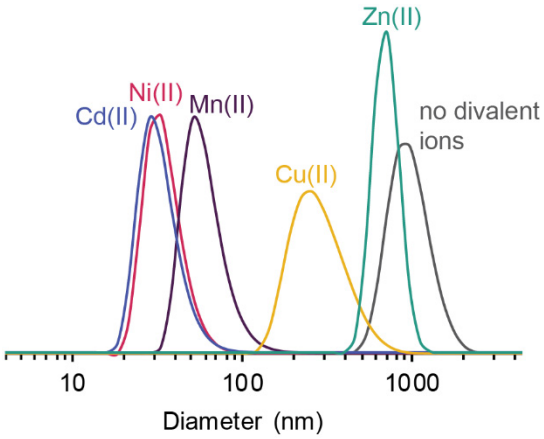

Figure S15. DLS number-average particle size distribution of the particles and particle aggregates formed in the presence of the listed ions (15 mM divalent ion).

References.

(1) Smirnov, I. P.; Zhu, X.; Taylor, T.; Huang, Y.; Ross, P.; Papayanopoulos, I. A.; Martin, S. A.; Pappin, D. J. *Anal. Chem.* **2004**, *76*, 2958-2965.

(2) Booth, D. S.; Avila-Sakar, A.; Cheng, Y. *J. Vis. Exp.* **2011**, *No. 58*, e3227.

(3) Ludtke, S. J., Baldwin, P. R. & Chiu, W. *J. Struct. Biol.* **1999**, *128*,, 82–97.